


LETTER TO THE EDITOR

Nitrogen fractionation in ammonia and its insights into nitrogen chemistry

E. Redaelli¹ , L. Bizzocchi², P. Caselli¹, and J. E. Pineda¹

¹ Centre for Astrochemical Studies, Max-Planck-Institut für extraterrestrische Physik, Gießenbachstraße 1, 85749 Garching bei München, Germany
e-mail: eredaelli@mpe.mpg.de

² Dipartimento di Chimica “Giacomo Ciamician”, Università di Bologna, Via F. Selmi 2, 40126 Bologna, Italy

Received 13 April 2023 / Accepted 29 May 2023

ABSTRACT

Context. Observations of the nitrogen isotopic ratio $^{14}\text{N}/^{15}\text{N}$ in the interstellar medium are becoming more frequent thanks to increased telescope capabilities. However, interpreting these data is still puzzling. In particular, measurements of $^{14}\text{N}/^{15}\text{N}$ in diazenylium have revealed high levels of anti-fractionation in cold cores, which is challenging to explain.

Aims. By using astrophysical simulations coupled with a gas-grain chemical code, it has been suggested that the ^{15}N -depletion in prestellar cores could be inherited from the initial stages, when $^{14}\text{N}^{15}\text{N}$ is selectively photodissociated and ^{15}N atoms deplete onto the dust grain, forming ammonia ices. Our aim is to test this hypothesis.

Methods. We targeted three sources (the prestellar core L1544, the protostellar envelope IRAS4A, and the shocked region L1157-B1) with distinct degrees of desorption or sputtering of the ammonia ices. We observed the ammonia isotopologues with the Green Bank Telescope, and we inferred the ammonia $^{14}\text{N}/^{15}\text{N}$ via spectral fitting of the observed inversion transitions.

Results. $^{15}\text{NH}_3$ (1,1) is detected in L1544 and IRAS4A, whilst only upper limits are deduced in L1157-B1. The NH_3 isotopic ratio is significantly lower towards the protostar ($^{14}\text{N}/^{15}\text{N} = 210 \pm 50$) than at the centre of L1544 ($^{14}\text{N}/^{15}\text{N} = 390 \pm 40$), where it is consistent with the elemental value. We also present the first spatially resolved map of NH_3 nitrogen isotopic ratio towards L1544.

Conclusions. Our results are in agreement with the hypothesis that ammonia ices are enriched in ^{15}N , leading to a decrease in the $^{14}\text{N}/^{15}\text{N}$ ratio when the ices are sublimated back into the gas phase for instance due to the temperature rise in protostellar envelopes. The ammonia $^{14}\text{N}/^{15}\text{N}$ value at the centre of L1544 is a factor of 2 lower than that of N_2H^+ , which can be explained if a significant fraction of nitrogen remains in atomic form and if the ammonia formed on the dust grains is released in the gas phase via non-thermal desorption.

Key words. astrochemistry – ISM: clouds – ISM: molecules – stars: formation – molecular processes

1. Introduction

The nitrogen (N) isotopic ratio $^{14}\text{N}/^{15}\text{N}$ is considered an important diagnostic tool to follow the evolution from the primitive Solar Nebula to the present time. In the Solar System, $^{14}\text{N}/^{15}\text{N}$ values range from values of ≈ 440 – 450 in the Jovian atmosphere and in the solar wind (Fouchet et al. 2004; Marty et al. 2011), which are believed to be representative of the Protosolar Nebula, to $^{14}\text{N}/^{15}\text{N} = 272$ in the Earth’s atmosphere (Nier 1950), down to isotopic ratios as low as 50 in local spots of carbonaceous chondrites (Bonafant et al. 2010). This evidence is likely indicative of the presence of multiple nitrogen reservoirs at the moment of the formation of the planetary system (cf. Hily-Blant et al. 2017; Grewal et al. 2021).

In the interstellar medium (ISM), measurements of the $^{14}\text{N}/^{15}\text{N}$ ratio are spread depending on the kind of source and on the targeted molecular tracer. Nitriles are usually enriched in ^{15}N with respect to the elemental value of 400, with $^{14}\text{N}/^{15}\text{N}$ values of 140–360 and of 160–460 in low-mass prestellar and protostellar cores, respectively (Hily-Blant et al. 2013; Wampfler et al. 2014). Spezzano et al. (2022) reported the first $^{14}\text{N}/^{15}\text{N}$ map in HCN in a prestellar core, and their results

show the importance of selective photodissociation in driving the nitrogen isotopic ratio of nitriles.

In low-mass prestellar sources, N_2H^+ appears instead deficient in ^{15}N , with isotopic ratios of $^{14}\text{N}/^{15}\text{N} = 580$ – 1000 (Bizzocchi et al. 2013; Redaelli et al. 2018). A possible explanation for these pieces of evidence was proposed by Loison et al. (2019), invoking an isotope dependency of the reaction rate for dissociative recombination (DR) of diazenylium. Due to this, in the cold ($T \lesssim 10$ K) and dense ($n \gtrsim 10^4$ cm $^{-3}$) gas, where CO is depleted and DR is the main destruction route for diazenylium, N^{15}NH^+ is destroyed faster than the main isotopologue, leading to high $^{14}\text{N}/^{15}\text{N}$ values. This theory found partial confirmation in the work of Redaelli et al. (2020), where the authors showed that $\text{N}_2\text{H}^+/\text{N}^{15}\text{NH}^+$ ratios in a sample of protostellar sources are significantly lower than in prestellar cores, suggesting that once CO dominates the destruction of N_2H^+ , its nitrogen isotopic ratio decreases back to the elemental value of ≈ 400 .

Furuya & Aikawa (2018), on the other hand, proposed that the ^{15}N antifractionation of diazenylium is inherited from the initial stages of the contraction when UV photons can still penetrate the cloud. At that time N_2 is selectively photodissociated, leading to a ^{15}N enrichment in the atomic nitrogen (NI) gas. As

the temperature decreases and density increases, N I freezes out onto the dust grains, where it rapidly reacts with hydrogen and leads to the formation of highly ^{15}N enriched ammonia ices. On the other hand, the adsorbed N_2 does not significantly react. As long as the N_2 non-thermal desorption rate is higher than the NH_3 rate, the net effect is that the bulk gas results depleted in heavy nitrogen, while the NH_3 ices are enriched. The direct consequence of this model is that, once the ammonia ices are evaporated back into the gas phase, we would expect to observe a lower $^{14}\text{NH}_3/^{15}\text{NH}_3$ ratio with respect to the prestellar phases.

To the best of our knowledge, in the local ISM $^{15}\text{NH}_3$ detection has been reported only in Barnard 1 and NGC 1333 (Lis et al. 2010)¹, with $^{14}\text{N}/^{15}\text{N} = 334 \pm 50$ (Barnard 1) and 344 ± 173 (NGC 1333), which are consistent with the nitrogen isotopic ratio in the local interstellar medium (300–400; Hily-Blant et al. 2017; Kahane et al. 2018; Colzi et al. 2018). Gerin et al. (2009) reported a small sample of $^{14}\text{N}/^{15}\text{N}$ measurements in deuterated ammonia (NH_2D). Their results span the range of 270–800, but the double fractionation makes them more difficult to interpret, also due to the limited signal-to-noise ratio (S/N). In this Letter we report the detection of $^{15}\text{NH}_3$ towards the prestellar core L1544 and the protostellar core NGC 1333-IRAS4A (hereafter IRAS4A), and the non-detection in the shocked region L1157-B1. We also show the first map of $^{14}\text{N}/^{15}\text{N}$ in ammonia, obtained in L1544.

2. Source selection and observations

The sources targeted in this work were selected to span a range of physical conditions. L1544 is a cold and highly concentrated prestellar core, reaching at its centre $T \sim 7\text{ K}$ and $n \sim 10^7\text{ cm}^{-3}$ (Crapsi et al. 2007; Keto et al. 2015). It already shows signs of gravitational contraction, also well extended in its envelope (Crapsi et al. 2005; Redaelli et al. 2022). The uneven illumination from the interstellar radiation field might be responsible for its diversified chemistry (Spezzano et al. 2017). IRAS4A is a Class 0 young stellar object, powering collimated molecular outflows (cf. Lefloch et al. 1998). Based on the detection of several complex organic molecules, it has been classified as a hot corino (Bottinelli et al. 2004), where, as a consequence of the high temperatures ($\sim 100\text{ K}$), the ice mantles on the dust grains have begun to evaporate. L1157-B1 is the shock region associated with the bipolar outflows driven by the class 0 protostar IRAS 20386+6751. The shock causes the sputtering of the dust grains, releasing refractory and volatile materials back into the gas phase, leading to a rich chemistry (Bachiller et al. 2001; Arce et al. 2008; Fontani et al. 2014; Codella et al. 2017).

The observations were performed at the Green Bank Telescope (GBT) in Green Bank, West Virginia, in two runs in March 2019, using the *K*-band Focal Plane Array (KFPA) receiver, in combination with the VEratile GBT Astronomical Spectrometer (VEGAS) backend. We used observing mode 20, which allows the eight VEGAS spectrometers to be combined with the seven KFPA beams, using frequency switching (throw: 4.11 MHz). The achieved spectral resolution is 5.9 kHz ($\approx 0.08\text{ km s}^{-1}$ at 23 GHz). Four sub-bands were centred on the lines of interest: NH_3 (1,1) at 23.694 GHz, NH_3 (2,2) at 23.722 GHz, $^{15}\text{NH}_3$ (1,1) at 22.624 GHz, and $^{15}\text{NH}_3$ (2,2) at 22.650 GHz.

¹ Chen et al. (2021) also reported $^{15}\text{NH}_3$ (1,1) detections in Barnard-1b and NGC 1333, and the derived isotopic ratios are consistent within the error bars with those of Lis et al. (2010).

The data were acquired as small daisy maps with radius $2'$ (first run) and $0'.75$ (second run). Mars and Venus were used as flux calibrators, and nodding observations (rotating among the seven beams) were used also to check the relative gains of the different beams. The data reduction was performed with the standard GBT KFPA pipeline (Masters et al. 2011). The beam and aperture efficiencies were set at 0.95 and 0.69, respectively, in order to calibrate the data in the main-beam temperature scale. The imaging of the data was performed with GBTGRIDDER². The data were gridded to a final pixel size of $6''$. At this stage, spectral smoothing was applied, downgrading the spectral resolution to $\approx 0.15\text{ km s}^{-1}$, in order to improve the S/N. The final beam size is $\approx 36''$.

The noise levels reached in the 0.15 km s^{-1} channel for the main isotopologues are rms = 20 mK (L1544), 40 mK (IRAS4A), and 30 mK (L1157-B1). For the $^{15}\text{NH}_3$ (1,1) line the datacubes present typical averages of rms $\approx 30\text{ mK}$. The $^{15}\text{NH}_3$ (2,2) line is not detected in any source. The integrated intensity maps for the main isotopologues, and for $^{15}\text{NH}_3$ towards L1544 are presented in Appendix A. In this work we focus only on the central region of each source (radius: $120''$), where the noise in the datacubes is approximately constant.

3. Analysis

Our main goal is to infer the nitrogen isotopic ratio $^{14}\text{N}/^{15}\text{N}$ from the column densities of the two ammonia isotopologues. These are derived by performing a spectral fit to the observed spectra, which is described in detail in Appendix B. In the following subsections we describe the results for each source.

3.1. L1544

We extract the spectra of all detected transitions in the central beam ($36''$) around the millimetre dust peak in order to improve the S/N of the $^{15}\text{NH}_3$ (1,1) line. The resulting data, together with the best fit obtained with PYSPECKIT, are shown in the top row of Fig. 1, and the best-fit solution is presented in Table 1. The V_{lsr} of the two species are consistent within uncertainties, which suggests that they arise from the same region in the source. However, it is important to note that the σ_V of $^{15}\text{NH}_3$ is larger than, and marginally inconsistent with, that of the main isotopologue. With the column density values derived, we obtain an isotopic ratio of $^{14}\text{N}/^{15}\text{N} = 390 \pm 40$.

3.2. IRAS4A

The $^{15}\text{NH}_3$ (1,1) line is undetected with the obtained rms level towards IRAS4A. In order to obtain a tentative detection at the 2σ level, we compute the average spectra in a central area of $45''$ of radius, shown in Fig. 1. We initially perform a single velocity-component spectral fit, shown in the middle row of panels in Fig. 1. The obtained best-fit parameters are summarised in Table 1. Using the obtained values for the column densities of the two isotopologues, we compute the isotopic ratio of $^{14}\text{N}/^{15}\text{N} = 260 \pm 50$.

The best-fit solution for the NH_3 transitions is unable to reproduce the spectral feature seen in the observations and in particular the blue shoulder at low velocities (see Fig. 1). This feature was also detected by Lis et al. (2010), and it is likely due to the blue lobe of the protostellar outflow, which enters

² Publicly available at <https://github.com/GreenBankObservatory/gbtgridded>

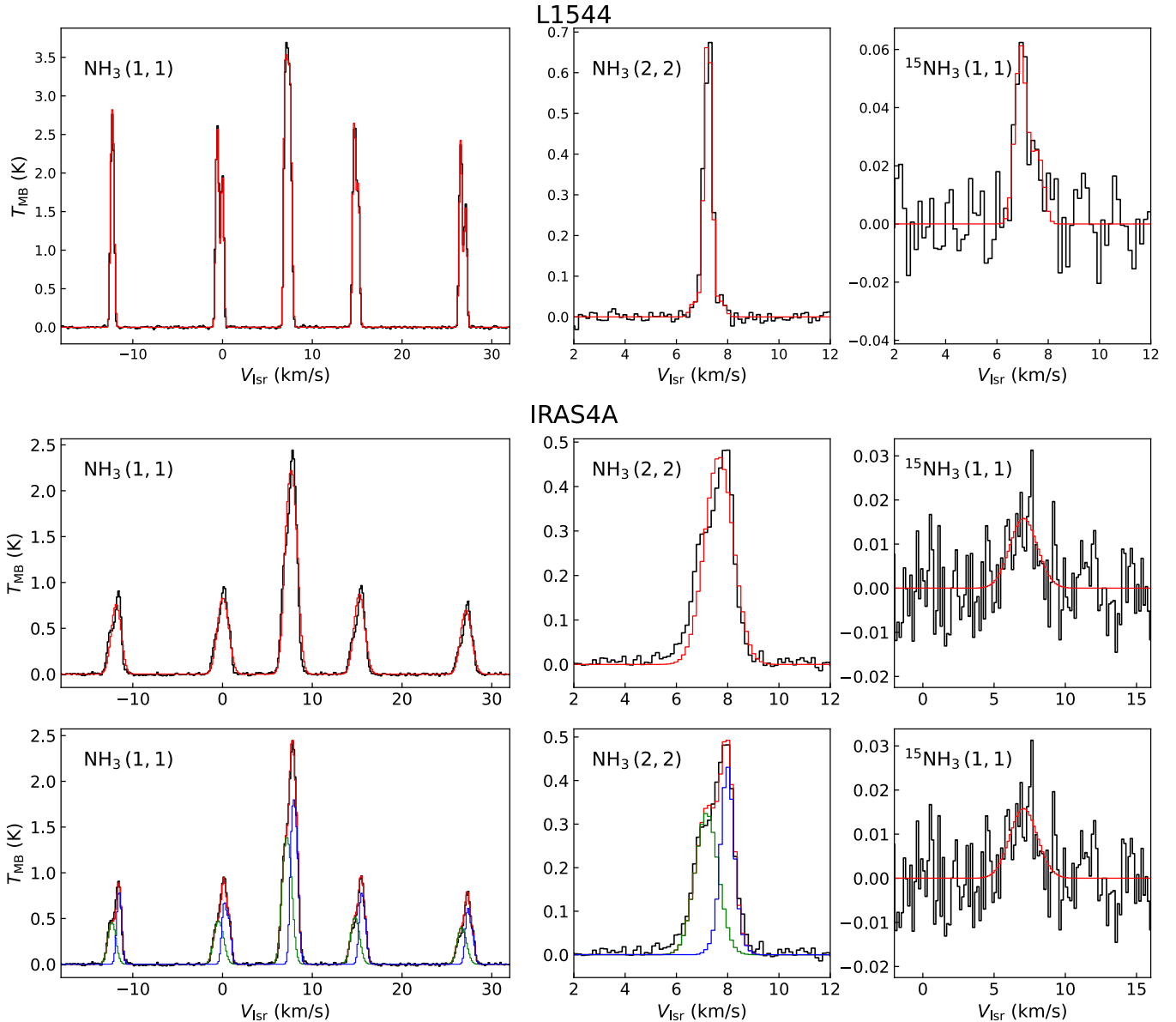


Fig. 1. Detected ammonia inversion transitions in the central beams (black histograms). Shown from left to right are NH_3 (1,1), NH_3 (2,2) (central main hyperfine group only), and $^{15}\text{NH}_3$ (1,1). In each panel the coloured histograms show the best-fit results. Top row: spectra extracted in central beam at dust peak of L1544. Centre row: same as the top row, but for IRAS4A. The spectra are averages over the central $90''$. The best-fit models obtained using a single velocity-component approach are shown with red histograms. Bottom row: left and central panels show the results of the two-component fit performed on the NH_3 lines in IRAS4A. The two velocity-components are shown in green (warmer component) and blue (colder component), whilst the total spectrum is shown in red. In the right panel the red curve shows the one-component fit to the $^{15}\text{NH}_3$ line, using the warmer component fit results as input for the temperature values.

the large GBT beam and the spatial average we performed. We then modelled the NH_3 lines using two velocity-components, and these results are also reported in Fig. 1 and Table 1. The total NH_3 emission is due to two contributions, a warmer component with $T_{\text{rot}} = (13.22 \pm 0.11)$ K at lower V_{LSR} , and a colder component characterised by higher V_{LSR} and lower temperature, $T_{\text{rot}} = (11.97 \pm 0.09)$ K. Although the temperature difference is only ~ 1.2 K, the velocity dispersion of the colder component is almost half that of the warmer one, supporting the scenario that its emission arises in the colder and more quiescent gas surrounding the hot corino. The V_{LSR} of the warmer component (7.1 km s^{-1}) is consistent with high-resolution line observations of the hot corino (see e.g., Bottinelli et al. 2004; Choi et al. 2011; Yamato et al. 2022, who all reported systemic velocities

of $6\text{--}7 \text{ km s}^{-1}$), further supporting the idea that this component arises from the warmer gas closer to the central protostar. The improvement of the fit using two velocity-components has been confirmed with the Akaike information criterion (e.g., as done by Choudhury et al. 2021; see Appendix C).

The low S/N $^{15}\text{NH}_3$ (1,1) spectrum prevents fitting two velocity-components. The best-fit solution for the one-component fit is found at $V_{\text{LSR}} = (7.2 \pm 0.2) \text{ km s}^{-1}$, which is inconsistent with the result of the single-component fit to the NH_3 lines, and it is instead consistent with the velocity of the warmer component (see Table 1). The $^{15}\text{NH}_3$ (1,1) line appears significantly broader than both velocity-components, but its linewidth is closer to that of the warmer component. We can thus speculate that the emission of the rarer isotopologues

Table 1. Best-fit solutions obtained for NH₃ and ¹⁵NH₃ lines towards L1544 and IRAS4A.

Species	T_{rot} (K)	T_{ex} (K)	$\log_{10} [N_{\text{col}}]$ ($\log_{10}[\text{cm}^{-2}]$)	σ_{v} (km s^{-1})	V_{lsr} (km s^{-1})
L1544					
NH ₃	8.74 ± 0.06	6.322 ± 0.016	14.970 ± 0.003	0.1464 ± 0.0006	7.1603 ± 0.0007
¹⁵ NH ₃	8.74	6.322	12.38 ± 0.05	0.20 ± 0.04	7.20 ± 0.04
IRAS4A – 1 component					
NH ₃	12.55 ± 0.16	6.07 ± 0.11	14.715 ± 0.012	0.528 ± 0.006	7.585 ± 0.005
¹⁵ NH ₃	12.55	6.07	12.31 ± 0.08	0.9 ± 0.2	7.2 ± 0.2
IRAS4A – 2 components					
NH ₃ warmer component	13.22 ± 0.11	5.08 ± 0.07	14.474 ± 0.012	0.423 ± 0.008	7.107 ± 0.013
NH ₃ colder component	11.97 ± 0.09	5.06 ± 0.07	14.522 ± 0.006	0.245 ± 0.003	7.915 ± 0.004
¹⁵ NH ₃	13.22	5.08	12.39 ± 0.08	0.9 ± 0.2	7.2 ± 0.2

Notes. For the latter, two sets of values are reported, corresponding to the one-component and two-component approaches (see main text for more details).

arises mostly from the warm gas closer to the central object. We re-fitted the ¹⁵NH₃ (1,1) line using the temperatures of the warmer component as fixed parameters. The nitrogen isotopic ratio regarding only the warmer component is $^{14}\text{N}/^{15}\text{N} = 210 \pm 50$.

3.3. L1157-B1

The ¹⁵NH₃ (1,1) line is undetected at the shock position L1157-B1. The main isotopologue lines present broad and asymmetric line profiles, with extended blue wings, due to the presence of the outflow and the shock. In order to estimate a lower limit on the nitrogen isotopic ratio, we used the results of Umemoto et al. (1999), who reported the detection of the first six inversion transition in the source and estimated the column density using the rotational diagram method³. The noise level in the ¹⁵NH₃ spectrum extracted from the central 72'' (equal to the beam size of the Nobeyama telescope used in Umemoto et al. 1999) is rms = 7 mK. Using the optically thin approximation (see Appendix A of Caselli et al. 2002), and assuming a line Full-Width-at-Half-Maximum of $FWHM = 1 \text{ km s}^{-1}$, we obtain an upper limit of $N_{\text{col}}(^{15}\text{NH}_3) \leq 6 \times 10^{11} \text{ cm}^{-2}$ and a lower limit on the isotopic ratio of $^{14}\text{N}/^{15}\text{N} \geq 160$.

3.4. $^{14}\text{N}/^{15}\text{N}$ map in L1544

The ¹⁵NH₃ line towards L1544 is bright enough to infer a map of the nitrogen isotopic ratio in ammonia, the first of its kind in an astrophysical source to our knowledge. The map, shown in the central panel of Fig. 2, is derived following the procedure described in Appendix B. Despite its small extension, some spatial trends can be seen. The isotopic ratio is higher at higher column densities. The average value for positions where $N(\text{H}_2) > 2 \times 10^{22} \text{ cm}^{-2}$ is $^{14}\text{N}/^{15}\text{N} = 390 \pm 60$, where the uncertainties are the standard deviation across the mean value. The ratio decreases at lower column densities, as visible in particular in the south-east direction, where its range is 150–250.

In order to confirm this spatial trend with higher S/N, we computed the average spectra over one beam at three different offsets (also shown in Fig. 2). The first offset (labelled A) is

centred in the N(H₂) peak⁴. Offsets B and C were chosen to cover approximately the same N(H₂) values in the south-east and north-west direction, respectively. The isotopic ratios obtained fitting the average NH₃ and ¹⁵NH₃ spectra are 420 ± 50 in A, 200 ± 40 in B, and 290 ± 70 in C. The difference of the isotopic ratios between A and B is significant above the 3σ level (220 ± 60), whilst that between A and C is instead detected only at 1.5σ level (130 ± 90). Based on these results, we can certainly confirm a decrease in $^{14}\text{N}/^{15}\text{N}$ in the south-eastern direction.

The ammonia $^{14}\text{N}/^{15}\text{N}$ map is strikingly similar to that of HCN reported by Spezzano et al. (2022) both regarding the morphology and the absolute values. Those authors also found a significant decrease in $^{14}\text{N}/^{15}\text{N}$ (although only in the south-eastern direction), from $^{14}\text{N}/^{15}\text{N} = 440 \pm 60$ at the core's centre down to 220 ± 30 towards a position close to offset B in Fig. 2.

4. Discussion and conclusions

In this work, we have measured the ammonia nitrogen isotopic ratio $^{14}\text{N}/^{15}\text{N}$ towards three sources, a prestellar core (L1544), a Class 0 protostar (IRAS4A), and the shocked region L1157-B1. The first result is that at the centre of L1544, where the temperature is the lowest in the sample ($T_{\text{rot}} \lesssim 9 \text{ K}$), the measured ratio is 390 ± 40 , significantly higher than the value in IRAS4A, where, using a two-component fit for the main isotopologue, we obtained $^{14}\text{N}/^{15}\text{N} = 210 \pm 50$, which is consistent with the results of Lis et al. (2010) (who pointed the telescope $\approx 20''$ away from our pointing). The difference between the two sources is $^{14}\text{N}/^{15}\text{N}_{\text{L1544}} - ^{14}\text{N}/^{15}\text{N}_{\text{IRAS4A}} = 180 \pm 60$, significant at the 3σ level. In L1157-B1, ¹⁵NH₃ is undetected, yielding to a lower limit ratio ≥ 160 . These results are in agreement with the scenario where gas-phase ammonia present an isotopic ratio close to the elemental value of ≈ 400 in cold and quiescent sources (L1544). The ammonia ices are instead enriched in ¹⁵N, and this enrichment is detected in the gas phase when the icy mantles are either evaporated due to the increase in temperature or destroyed by shocks. These findings would hence support the theory of Furuya & Aikawa (2018).

This work provides the first spatially resolved ammonia $^{14}\text{N}/^{15}\text{N}$ map. At the centre of the prestellar core L1544, the obtained $^{14}\text{N}/^{15}\text{N}$ is consistent both with the Protosolar Nebula

³ The strong asymmetry in the spectra prevent us from using the local thermal equilibrium fit implemented in PYSPECKIT.

⁴ The N(H₂) map is computed from *Herschel* data, and its peak is shifted by $\approx 10''$ with respect to the millimetre dust peak at which the spectra of Fig. 1 are taken.

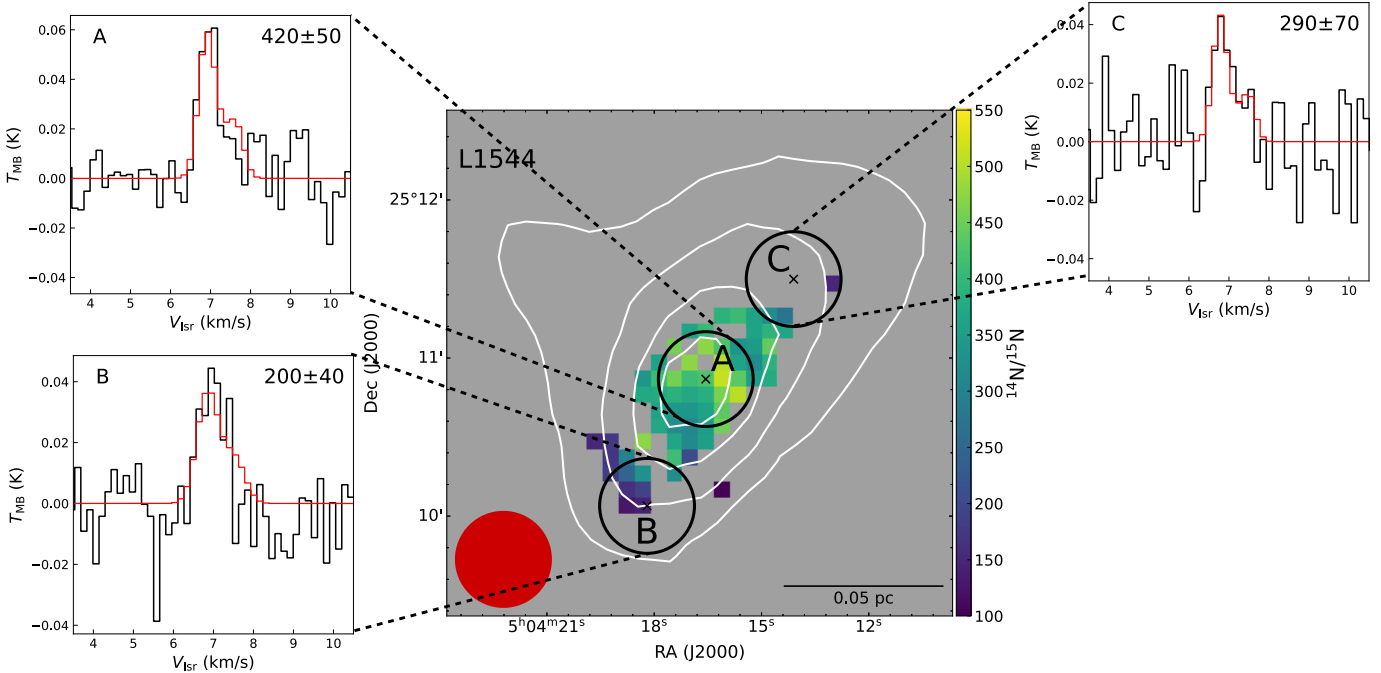


Fig. 2. Results of the analysis of the ammonia maps in L1544. Central panel: ammonia $^{14}\text{N}/^{15}\text{N}$ map. The contours show the total gas density at levels $N(\text{H}_2) = [1, 1.5, 2, 2.5] \times 10^{22} \text{ cm}^{-2}$, obtained from *Herschel* SED fitting (Spezzano et al. 2017). The black circles show the three offsets (labelled with capital letters) where we compute average spectra to improve the S/N. The averaged $^{15}\text{NH}_3$ (1,1) lines are shown in the surrounding panels (black: observations, red: best-fit models, obtained as described in Appendix B). These panels are labelled in their top left corner, whilst in the top right corners we indicate the measured $^{14}\text{N}/^{15}\text{N}$.

value and with the elemental value in the local ISM. On the other hand, it is almost a factor of two lower than that of N_2H^+ , derived using single-dish data at a similar resolution ($\text{N}_2\text{H}^+/\text{N}^{15}\text{NH}^+ = 920_{-200}^{+300}$, Redaelli et al. 2018). This can be explained if a significant fraction of nitrogen is in atomic form also in the high-density and low-temperature centre of prestellar cores, as suggested by Maret et al. (2006), and if NH_3 can efficiently form on the surface of dust grains (via hydrogenation of atomic nitrogen), followed by reactive desorption. As NH_3 formation in the gas phase starts from the reaction $\text{N}_2 + \text{He}^+ \rightarrow \text{N} + \text{N} + \text{He}$, and given that N_2 is ^{15}N -deficient towards the core centre (as measured by N_2H^+), the same antifractionation should be found in NH_3 . As this is not the case, atomic ^{15}N -enrichment is needed to allow the ^{15}N -fractionation of NH_3 to reach the ISM values (i.e., about a factor of two higher than that of N_2H^+). One possible explanation is that a significant fraction of the nitrogen is still in the atomic form in the core centre, maintaining a low $^{14}\text{N}/^{15}\text{N}$ value due to selective photodissociation of N^{15}N . The ^{15}N enrichment is then transmitted to ammonia forming on the dust grains, from where it can be desorbed through reactive desorption. This is especially true towards the south of L1544, which is more exposed to the interstellar radiation field (cf. Spezzano et al. 2016) favouring the selective photodissociation, where we detect a decrease in $^{14}\text{N}/^{15}\text{N}$. The fact that ammonia mainly comes from the surface hydrogenation of atomic nitrogen would also explain the similarities between the $^{14}\text{N}/^{15}\text{N}$ map of NH_3 and of HCN (cf. Spezzano et al. 2022), as nitriles are formed from atomic nitrogen also in the gas phase. A further element to take into consideration is that at the core centre, the abundance of He^+ increases due to the CO catastrophic freeze-out (see e.g., Sipilä et al. 2019), thus making the gas-phase formation route more efficient and then decreasing the ^{15}N -fractionation. Recent works have revealed that ammonia

isotopologues suffer from depletion at the high densities characteristic of dense prestellar cores ($n > 10^5 \text{ cm}^{-3}$), which however can be seen only with high-resolution interferometric data (e.g., the core H-MM1 seen with Very Large Array, Pineda et al. 2022; or L1544 observed with the Atacama Large millimeter/submillimeter Array, Caselli et al. 2022). We exclude hence that this phenomenon is important at the scales probed by our GBT data.

Another possible explanation to this observational evidence is that the N_2H^+ isotopic ratio is not tracing the bulk of N_2 gas, due to isotope-selective dissociative recombination (as suggested by Loison et al. 2019). The $^{14}\text{N}/^{15}\text{N}$ measurement in N_2H^+ is available only at the dust peak, however, preventing us from drawing conclusions on the meaning of the NH_3 isotopic ratio towards the south-east of the core in this scenario (beyond that already discussed). Laboratory results testing this hypothesis are needed to confirm whether the nitrogen isotopic ratio of N_2H^+ is indeed indicative of that of molecular nitrogen, or if it experiences other fractionation processes.

Our results show that significant efforts are still necessary to understand nitrogen chemistry. The derived $^{14}\text{N}/^{15}\text{N}$ values also show that non-thermal desorption mechanisms are important and must be taken into account in astrochemical models.

Acknowledgements. The authors kindly thank the anonymous referee for the comments that helped improve the manuscript. ER, PC, and JEP acknowledge the support of the Max Planck Society. ER thanks Dr. J. Chantzou, for the help and support during the data acquisition.

References

Arce, H. G., Santiago-García, J., Jørgensen, J. K., Tafalla, M., & Bachiller, R. 2008, *AJ*, 681, L21

- Bachiller, R., Martin-Pintado, J., & Fuente, A. 1993, *ApJ*, **417**, L45
- Bachiller, R., Pérez Gutiérrez, M., Kumar, M. S. N., & Tafalla, M. 2001, *A&A*, **372**, 899
- Bizzocchi, L., Caselli, P., Leonardo, E., & Dore, L. 2013, *A&A*, **555**, A109
- Bonal, L., Huss, G. R., Krot, A. N., et al. 2010, *Geochim. Cosmochim. Acta*, **74**, 6590
- Bottinelli, S., Ceccarelli, C., Lefloch, B., et al. 2004, *ApJ*, **615**, 354
- Caselli, P., Walmsley, C. M., Zucconi, A., et al. 2002, *ApJ*, **565**, 344
- Caselli, P., Pineda, J. E., Sipilä, O., et al. 2022, *ApJ*, **929**, 13
- Chen, J. L., Zhang, J. S., Henkel, C., et al. 2021, *ApJS*, **257**, 39
- Choi, M., Kang, M., Tatematsu, K., Lee, J.-E., & Park, G. 2011, *PASJ*, **63**, 1281
- Choudhury, S., Pineda, J. E., Caselli, P., et al. 2021, *A&A*, **648**, A114
- Codella, C., Ceccarelli, C., Caselli, P., et al. 2017, *A&A*, **605**, L3
- Colzi, L., Fontani, F., Rivilla, V. M., et al. 2018, *MNRAS*, **976**,
- Crapsi, A., Caselli, P., Walmsley, C. M., et al. 2005, *ApJ*, **619**, 379
- Crapsi, A., Caselli, P., Walmsley, M. C., & Tafalla, M. 2007, *A&A*, **470**, 221
- Fontani, F., Codella, C., Ceccarelli, C., et al. 2014, *ApJ*, **788**, L43
- Fouchet, T., Irwin, P. G. J., Parrish, P., et al. 2004, *Icarus*, **172**, 50
- Friesen, R. K., Pineda, J. E., co-PIs, , et al. 2017, *ApJ*, **843**, 63
- Furuya, K., & Aikawa, Y. 2018, *ApJ*, **857**, 105
- Galli, P. A. B., Loinard, L., Bouy, H., et al. 2019, *A&A*, **630**, A137
- Gerin, M., Marcelino, N., Biver, N., et al. 2009, *A&A*, **498**, L9
- Ginsburg, A., & Mirocha, J. 2011, Astrophysics Source Code Library [record ascl:[1109.001](#)]
- Ginsburg, A., Sokolov, V., de Val-Borro, M., et al. 2022, *AJ*, **163**, 291
- Grewal, D. S., Dasgupta, R., & Marty, B. 2021, *Nat. Astron.*, **5**, 356
- Hily-Blant, P., Bonal, L., Faure, A., & Quirico, E. 2013, *Icarus*, **223**, 582
- Hily-Blant, P., Magalhaes, V., Kastner, J., et al. 2017, *A&A*, **603**, L6
- Hirota, T., Bushimata, T., Choi, Y. K., et al. 2008, *PASJ*, **60**, 37
- Hougen, J. T. 1972, *J. Chem. Phys.*, **57**, 4207
- Kahane, C., Jaber Al-Edhari, A., Ceccarelli, C., et al. 2018, *ApJ*, **852**, 130
- Keto, E., Caselli, P., & Rawlings, J. 2015, *MNRAS*, **446**, 3731
- Kukolich, S. G. 1967, *Phys. Rev.*, **156**, 83
- Kukolich, S. G. 1968, *Phys. Rev.*, **172**, 59
- Lefloch, B., Castets, A., Cernicharo, J., Langer, W. D., & Zylka, R. 1998, *A&A*, **334**, 269
- Lis, D. C., Wootten, A., Gerin, M., & Roueff, E. 2010, *ApJ*, **710**, L49
- Loison, J.-C., Wakelam, V., Gratier, P., & Hickson, K. M. 2019, *MNRAS*, **484**, 2747
- Maret, S., Bergin, E. A., & Lada, C. J. 2006, *Nature*, **442**, 425
- Marty, B., Chaussidon, M., Wiens, R. C., Jurewicz, A. J. G., & Burnett, D. S. 2011, *Science*, **332**, 1533
- Masters, J., Garwood, B., Langston, G., & Shelton, A. 2011, in *Astronomical Data Analysis Software and Systems XX*, eds. I. N. Evans, A. Accomazzi, D. J. Mink, & A. H. Rots, *ASP Conf. Ser.*, **442**, 127
- Navarro-Almaida, D., Bop, C. T., Lique, F., et al. 2023, *A&A*, **670**, A110
- Nier, A. O. 1950, *Phys. Rev.*, **77**, 789
- Pineda, J. E., Harju, J., Caselli, P., et al. 2022, *AJ*, **163**, 294
- Redaelli, E., Bizzocchi, L., Caselli, P., et al. 2018, *A&A*, **617**, A7
- Redaelli, E., Bizzocchi, L., & Caselli, P. 2020, *A&A*, **644**, A29
- Redaelli, E., Chacón-Tanarro, A., Caselli, P., et al. 2022, *ApJ*, **941**, 168
- Sipilä, O., Harju, J., Caselli, P., & Schlemmer, S. 2015, *A&A*, **581**, A122
- Sipilä, O., Caselli, P., Redaelli, E., Juvela, M., & Bizzocchi, L. 2019, *MNRAS*, **487**, 1269
- Spezzano, S., Bizzocchi, L., Caselli, P., Harju, J., & Brünken, S. 2016, *A&A*, **592**, L11
- Spezzano, S., Caselli, P., Bizzocchi, L., Giuliano, B. M., & Lattanzi, V. 2017, *A&A*, **606**, A82
- Spezzano, S., Caselli, P., Sipilä, O., & Bizzocchi, L. 2022, *A&A*, **664**, L2
- Swift, J. J., Welch, W. J., & Di Francesco, J. 2005, *ApJ*, **620**, 823
- Tafalla, M., & Bachiller, R. 1995, *ApJ*, **443**, L37
- Umamoto, T., Mikami, H., Yamamoto, S., & Hirano, N. 1999, *ApJ*, **525**, L105
- Wampfler, S. F., Jørgensen, J. K., Bizzarro, M., & Bisschop, S. E. 2014, *A&A*, **572**, A24
- Yamato, Y., Furuya, K., Aikawa, Y., et al. 2022, *ApJ*, **941**, 75

Appendix A: Integrated intensity maps for the detected transitions

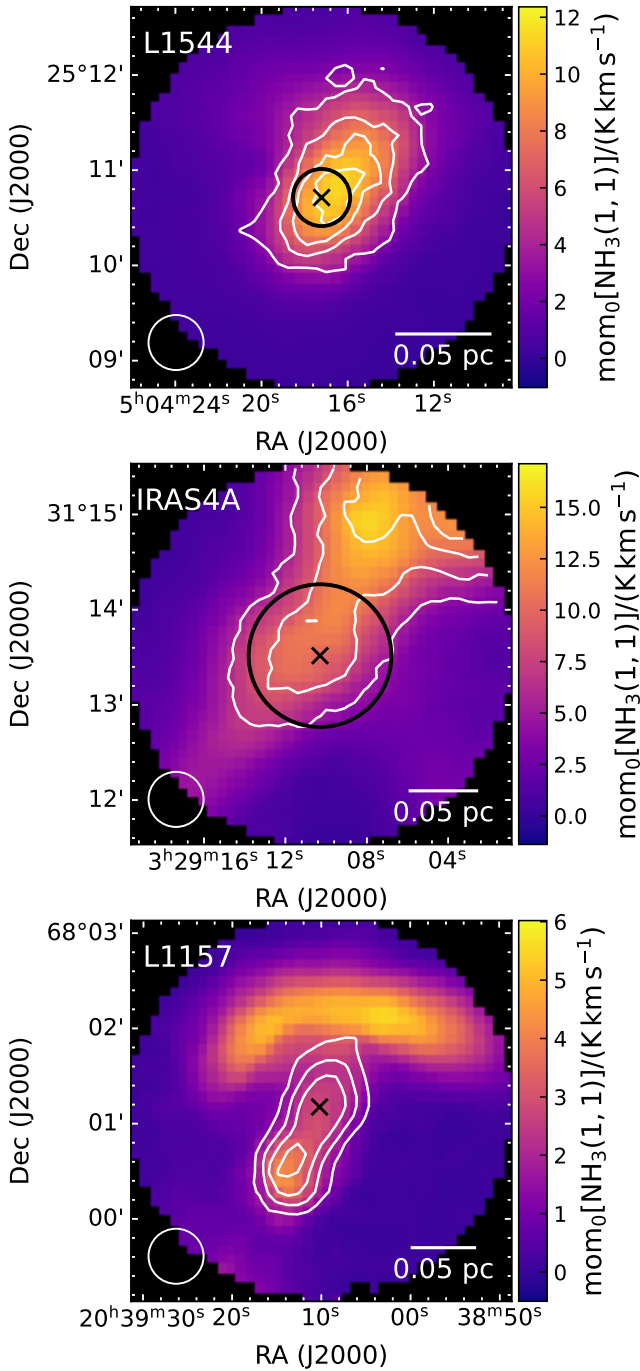


Fig. A.1. Each panel shows the integrated intensity of the NH_3 (1,1) line (see colour scale at right). The central pointings (see main text) are shown with a black cross. The contours show the integrated intensity of the corresponding (2,2) transition, at levels of 0.3, 0.5, 0.7, 0.9 of the peak value, which is 0.4 K km s^{-1} (L1544, top panel), 1.6 K km s^{-1} (IRAS4A, central panel), and 2.3 K km s^{-1} (L1157-B1, bottom panel). The beam size and scale bar are shown in the bottom left and right corners, respectively, of each panel. The black circles in the top and central panels show the areas where the spectra in Fig. 1 are extracted.

Figure A.1 presents the maps of the integrated intensity of the main isotopologues transitions towards the three targets: L1544

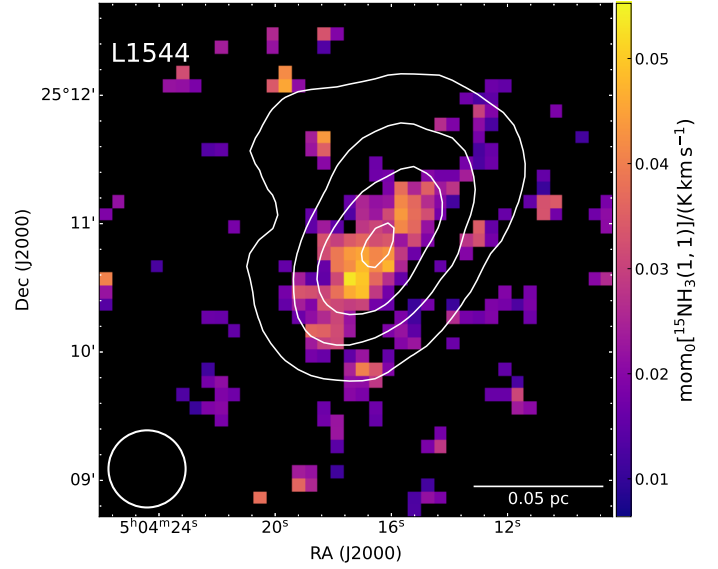


Fig. A.2. Integrated intensity of $^{15}\text{NH}_3$ (1,1) in L1544, masked following $S/N < 3$. The contours show the integrated intensity of the NH_3 (1,1) line. The levels start at 2 K km s^{-1} and increase with a step of 3 K km s^{-1} . The average noise level of the map is 6 mK km s^{-1} . The beam size and scale bar are shown in the bottom left and right corners, respectively.

(distance $d = 170 \text{ pc}$, Galli et al. 2019; coordinates $\alpha_{J2000} = 05^{\text{h}} 04^{\text{m}} 17^{\text{s}}.2$, $\delta_{J2000} = 25^{\circ} 10^{\text{m}} 41^{\text{s}}.8$), IRAS4A (distance $d = 235 \text{ pc}$, Hirota et al. 2008; coordinates $\alpha_{J2000} = 03^{\text{h}} 29^{\text{m}} 10^{\text{s}}.3$, $\delta_{J2000} = 31^{\circ} 13^{\text{m}} 31^{\text{s}}.0$), and L1157-B1 (distance $d = 250 \text{ pc}$, Arce et al. 2008; coordinates $\alpha_{J2000} = 20^{\text{h}} 39^{\text{m}} 10^{\text{s}}.2$, $\delta_{J2000} = 68^{\circ} 01^{\text{m}} 10^{\text{s}}.5$). These are computed by selecting the channels with line emission (i.e. considering all hyperfine components), and excluding channels with a noise level higher than 2σ . Uncertainties on the integrated intensity are computed as $rms_{\text{II}} = \sqrt{N_{\text{ch}}} \times \delta V \times rms$, where N_{ch} is the number of channels over which the integration is performed, and δV is the channel width. The resulting average uncertainties for the NH_3 (1,1) and (2,2) lines are 16 mK km s^{-1} and 6 mK km s^{-1} for L1544, 42 mK km s^{-1} and 20 mK km s^{-1} for IRAS4A, and 26 mK km s^{-1} and 15 mK km s^{-1} in L1157-B1.

The NH_3 emission in L1544 for both transitions shows a core-like structure, roughly centred around the dust peak. The core has an elliptical shape, with the major axis in the north-west–south-east direction. Towards IRAS4A, the two NH_3 lines show an elongated morphology, with a secondary peak close to the position on the hot corino. The intensity peaks, however, are found at the north-east limit of the field of view (FoV); this is consistent with larger scale maps of the region (see e.g. Friesen & Pineda 2017), which show a peak of NH_3 intensity in that direction. Towards L1157, the NH_3 (1,1) and (2,2) transitions present different morphology, due to the presence of the outflow and the associated shocks. The (1,1) integrated intensity presents a flattened structure in the north of the FoV, in correspondence with the dense core surrounding the protostar IRAS 20386+6751 (cf. Bachiller et al. 1993). A weaker emission is also seen along the blue-shifted outflow, towards the knots B1 (centre of the map in Fig. A.1) and B2 (immediately to the south-east of B1). The integrated intensity map of NH_3 (2,2) is instead dominated by the emission in the shocks along the outflow, which leads to increasing intensities and linewidths of this

transition (as also shown by Tafalla & Bachiller 1995, using the (1,1) and (3,3) transitions).

The $^{15}\text{NH}_3$ (1,1) is quite weak, reaching peak intensities of ≈ 60 mK at the centre of L1544, and of ≈ 20 mK at the centre of IRAS4A. The transition is not detected in L1157-B1. In the case of L1544, the line is bright enough to map its integrated intensity, and the result is shown in Fig. A.2.

Appendix B: Spectral fitting procedure

The spectral fit is performed using the PYTHON package PYSPECKIT, which already contains the full spectroscopic description of the NH_3 inversion transition (Ginsburg & Mirocha 2011; Ginsburg et al. 2022). In order to perform a consistent analysis of both isotopologues, we have recently updated the package to include the model for the $^{15}\text{NH}_3$ (1,1) and (2,2) lines. In particular, we took the frequencies, the rotational constants, and the Einstein coefficients for spontaneous emission values from the CDMS catalogue. We performed the calculations for the hyperfine structures, as follows. The component position and intensities of the hyperfine structure of the $^{15}\text{NH}_3$ $J_K = 1_1 - 1_1$ and $2_2 - 2_2$ transitions were computed from a complete reanalysis of the literature molecular beam data (Kukolich 1967, 1968; Hougen 1972). Such high-resolution (~ 0.3 kHz) measurements allowed the discrimination between subtle hyperfine effects and the determination of the coupling constants for ^{15}N and H spin-rotation, as well as ^{15}N -H, and H-H spin-spin coupling. The $^{15}\text{NH}_3$ $J_K = 1_1 - 1_1$ consists of 13 hyperfine components, labelled with the quantum numbers J, K, F , and I . The $J_K = 2_2 - 2_2$ full hyperfine structure is made of 14 components, with the central 4 components merged in a single unresolved feature.

The spectroscopic fit to the NH_3 lines is based on six free parameters: the local standard-of-rest velocity (V_{lsr}), the line velocity dispersion (σ_V), the total column density $N_{\text{col}}(\text{NH}_3)$, the excitation and rotational temperatures (T_{ex} and T_{rot}), and the ortho-to-para ratio. We fix the last to 1 since we have access only to para states, even though we are aware that models predict $OPR = 0.5$ for NH_3 (see e.g. Sipilä et al. 2015, fig 1.). Having detected two inversion transitions, both at high S/N, allows us to constrain the remaining five parameters.

For the rarer isotopologue, we only detect the first (1,1) line. We cannot, therefore, constrain all the parameters since they become degenerate, also because the hyperfine structure of the transition is very compact, and thus assessment of the line optical depth is challenging. When fitting this transition, we keep the rotational and excitation temperature fixed to the values derived from the main isotopologues. Only σ_V , V_{lsr} , and $N_{\text{col}}(^{15}\text{NH}_3)$ are then fit. Assuming that the two isotopologues emit from the same region, one could also fix the kinematic parameters (σ_V and V_{lsr}) of the rarer $^{15}\text{NH}_3$ to those of the main NH_3 . However, we prefer to keep them free, in order to investigate the analogies and differences between them. However we checked that the two approaches yield consistent results in terms of the isotopic ratio, within the uncertainties.

The assumption that T_{rot} is the same for the two isotopologues is not entirely correct, as the true constant quantity is the gas kinetic temperature T_K . This assumption, however, introduces negligible errors. The relation between T_{rot} and T_K is derived from assuming a three-level system formed only by the states (1,1), (2,2), and (2,1); it depends on the energy difference between the (1,1) and the (2,2) levels (which differs by less than 1% between NH_3 and $^{15}\text{NH}_3$) and on the ratio among the collisional coefficients $C_{2,2 \rightarrow 2,1}/C_{2,2 \rightarrow 1,1}$ (cf. Swift et al. 2005). The

$^{15}\text{NH}_3$ collisional coefficients are not available. However, we expect that they can differ at most by 10-15%; similar differences have been found in ^{15}N -bearing isotopologues of HNC and HCN (see Navarro-Almaida et al. 2023). Furthermore, for $T_K < 15$ K, $T_{\text{rot}} \approx T_K$ with a maximum difference of $< 10\%$.

The spectral fits yield, among the other parameters, the best-fit values and uncertainties for the column densities of the two isotopologues. The isotopic ratios are evaluated from the ratio of these column densities, and the associated uncertainties are computed using standard error propagation.

In order to produce the ammonia $^{14}\text{N}/^{15}\text{N}$ map in L1544 discussed in Sect. 3.4, we first selected the pixels where the integrated intensity of $^{15}\text{NH}_3$ (1,1) is above the 3σ level, and where the peak intensity of NH_3 (2,2) is detected above the 5σ level. The latter constraint aims at improving the estimates of the rotational temperature, and we then follow the same procedure as for the single pointing described in Sect. 3.1. We fit the main isotopologue transitions simultaneously, obtaining the maps of the rotational temperature, the excitation temperature, and NH_3 column density, among others. The first two maps are used as fixed parameters to fit the $^{15}\text{NH}_3$ (1,1) transition. The ratio of the column density maps of the two isotopologues yields the nitrogen isotopic ratio map shown in Fig. 2.

We highlight that the hypothesis that T_{ex} is the same for both isotopologues could be untrue if they are not tracing the same regions in the source. Assessing T_{ex} for the rarer isotopologue is not possible with the available data. We have, however, made a test, modifying the T_{ex} values of $^{15}\text{NH}_3$ by ± 1 K. The resulting isotopic ratios vary by 15 – 30%, which is comparable with the typical relative errors on $^{14}\text{N}/^{15}\text{N}$. Furthermore, the comparison between the distinct sources and the trends within L1544 still hold. We conclude that our results do not depend strongly on this assumption.

Appendix C: Akaike information criterion

The Akaike information criterion determines whether a model fit improves significantly when the number of free parameters is increased. To do so, the method computes the quantity

$$\text{AIC} = \chi^2 + C + 2n, \quad (\text{C.1})$$

where χ^2 is the chi-square of the model, n is the number of free parameters, and C is a constant that depends, basically, on the noise level in the data. When fitting a spectrum with one or two velocity-components, C does not change, whilst the number of free parameters changes from $n = 5$ to $n' = 10$. The relevant quantity is hence the AIC variation:

$$\Delta_{\text{AIC}} = \Delta\chi^2 + 2 \times (n' - n) = \Delta\chi^2 - 10. \quad (\text{C.2})$$

The smaller the AIC value, the better the fit. The χ^2 value for each fit is

$$\chi^2 = N_{\text{ch}} \times \frac{\sigma_{\text{res}}^2}{\text{rms}^2}, \quad (\text{C.3})$$

where σ_{res} is the standard deviation of the residuals of the fit, computed over the channels N_{ch} where the model with two components is $> 10^{-6}$ (in order to keep N_{ch} constant when varying the number of velocity-components), and $\text{rms} = 9$ mK is the noise, assumed to be constant in all channels. The AIC variation we compute when increasing the number of velocity-components is $\Delta_{\text{AIC}} = -19 \times 10^3$, hence the improvement of the fit is highly significant.